



## Continuous bridge displacement estimation using millimeter-wave radar, strain gauge and accelerometer

Zhanxiong Ma, Jaemook Choi, Hoon Sohn \*

Department of Civil and Environmental Engineering, Korea Advanced Institute of Science and Technology, Daejeon 34141, South Korea



### ARTICLE INFO

Communicated by Wei-Xin Ren

**Keywords:**

Continuous bridge displacement estimation  
Accelerometer  
Millimeter-wave radar  
Strain gauge  
Target occlusion  
Environmental variation

### ABSTRACT

Monitoring of bridge displacement is essential for providing critical information regarding the health of bridge structures. However, continuous and accurate monitoring of structural displacement remains challenging. This study proposes a bridge displacement estimation technique that combines an accelerometer, a strain gauge, and a millimeter-wave radar considering intermittent radar target occlusion common in long-term displacement monitoring. The technique primarily estimates displacement using radar and accelerometer measurements but switches to using strain and acceleration measurements when radar targets are occluded. A radar target occlusion detection algorithm is developed to automatically achieve this switching. Automated initial calibration is performed to select suitable targets from all radar-detected targets and estimate the conversion factor for converting radar-based displacement from the line-of-sight direction to the actual movement direction. An artificial neural network model is automatically trained for strain-displacement transformation without the need for any pre-knowledge of a target structure. The proposed technique was validated via a laboratory test on a 10-m-long beam-type structure and a field test on a pedestrian steel box-girder bridge. The proposed technique correctly detected the intermittent radar target occlusion, and continuously estimated displacements for up to 75 min. The intermittent radar target occlusion leads to errors of a few millimeters in the displacements estimated using radar and accelerometers. However, the proposed method accurately estimates displacements with errors of less than 0.1 mm.

### 1. Introduction

Displacement response is essential for bridge loading tests [1], modal identification [2], damage detection [3], and finite element model updating [4]. Contact-type techniques using linear variable differential transformers (LVDT) [5], accelerometers [6–8], strain gauges [9,10], and real-time kinematic global navigation satellite system (RTK-GNSS) [11,12], and noncontact techniques using laser Doppler vibrometers (LDV) [13], radar systems [14,15], and vision cameras [16–18] have been developed for directly measuring or indirectly estimating the bridge displacement. However, each of these sensors has its limitations. For example, accelerometers are not accurate for estimating low-frequency displacement, while strain-based displacements are noisy because of the high-level noise in strain measurements. Although radar systems are capable of high-accuracy and high-sampling displacement measurements, they are expensive and require rigid ground for installation, making them impractical for civil infrastructure purposes.

Efforts have been made to fuse different sensors for better displacement estimation [19,20]; among the fusion-based techniques,

\* Corresponding author.

E-mail addresses: [mazhanxiong@kaist.ac.kr](mailto:mazhanxiong@kaist.ac.kr) (Z. Ma), [cjmoock@kaist.ac.kr](mailto:cjmoock@kaist.ac.kr) (J. Choi), [hooonsohn@kaist.ac.kr](mailto:hooonsohn@kaist.ac.kr) (H. Sohn).

accelerometers are most commonly fused with other types of sensors, such as RTK-GNSS [21,22], vision cameras [23,24], strain gauges [25,26], and millimeter-wave radar systems [27]. However, in urban settings, the fusion of RTK-GNSS and accelerometer may result in low accuracy owing to multi-path errors; the fusion of vision camera and accelerometer cannot work in poor-illumination environments, such as at night, and the fusion of strain gauges and accelerometers may have large errors in long-term continuous monitoring owing to the zero-drift of strain measurement induced by environmental temperature variation and adverse heating caused by the electric current [28]. Although the fusion of millimeter-wave radar and accelerometer has a high accuracy and robustness to temperature and illumination variations, it cannot work well with intermittent target occlusion, which is common in long-term continuous displacement monitoring. Note that a temporary target occlusion will not only cause displacement loss during the occlusion but also cause a displacement drift after the target occlusion period owing to the phase unwrapping failure (Fig. 1).

By fusing a collocated accelerometer, strain gauge, and millimeter-wave radar, this study proposes a high-accuracy displacement estimation technique specifically for long-term continuous measurement of the vertical movement of a bridge structure (Fig. 2). Fig. 3 shows a flowchart of the proposed technique. First, the short-period initial measurements from three sensors were used to: (1) select multiple good targets and estimate their conversion factors for the millimeter-wave radar, and (2) train an artificial neural network (ANN) model for strain–displacement transformation (Section 3.1). Subsequently, the displacement was continuously estimated (Section 3.2). Depending on whether all the selected targets are occluded, all time steps can be categorized into three stages:

*Stage I-Radar target available:* with at least one of the selected targets available, the proposed technique first estimates a displacement from radar measurement with an acceleration-aided adaptive phase unwrapping algorithm, and then fuses the radar-based displacement with acceleration measurement using finite impulse response (FIR) filters for improved displacement estimation.

*Stage II- Radar target occlusion:* with all selected targets occluded, the proposed technique first estimates a displacement from strain measurements using the trained ANN model, and then fuses the strain-based displacement with acceleration measurement using FIR filters for improved displacement estimation.

*Stage III-Radar target recover:* with at least one of the selected targets recovered, the proposed technique switches to using radar and acceleration measurement for displacement estimation. A large drift in the radar-based displacement caused by radar target occlusion is eliminated using strain measurements. Other displacement estimation processes are the same as in Stage I.

The main contributions of this study are as follows: (1) a special emphasis is laid on the development of a bridge displacement estimation technique robust to intermittent radar target occlusion by fusing collocated millimeter-wave radar, strain gauge, and accelerometer; (2) an algorithm was developed to automatically detect the occurrence of target occlusion caused by moving objects, such as vehicles, and switch to an alternative stationary target available; and (3) even when all the potential stationary targets are occluded, bridge displacement is still reliably estimated by fusing strain and acceleration measurements without any prior knowledge of mode shapes or the neutral axis location.

The remainder of this paper is organized as follows. The research background is presented in section 2, and the working principle of the proposed technique is explained in section 3. The feasibility of the proposed technique was experimentally validated via tests on a 10-m-long beam-type structure and steel box-girder pedestrian bridge, as described in Sections 4 and 5, respectively. The concluding remarks are presented in Section 6.

## 2. Research background

### 2.1. Radar-based displacement estimation

Fig. 4 shows a flowchart of the radar-based displacement estimation. At the  $k^{\text{th}}$  time step, a millimeter-wave radar transmits a frequency-modulated signal ( $S_T(t)$ ) with duration of  $T_c$  [29],

$$S_T(t) = e^{i(2\pi f_s t + \pi Kt^2)} (k\Delta t \leq t \leq k\Delta t + T_c) \quad (1)$$

where  $f_s$  and  $K$  denote the starting frequency and the frequency slope of the frequency-modulated signal, respectively. The transmitted signal is reflected by multiple targets ( $Q$ ) in the surroundings of the radar, and the mixed signal ( $S_R(t)$ ) of these reflected signals is obtained as follows:

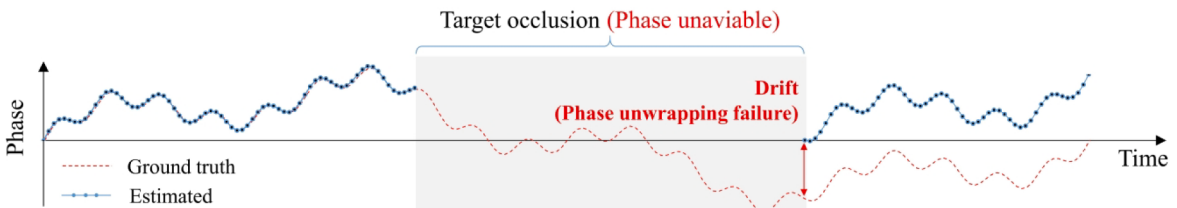
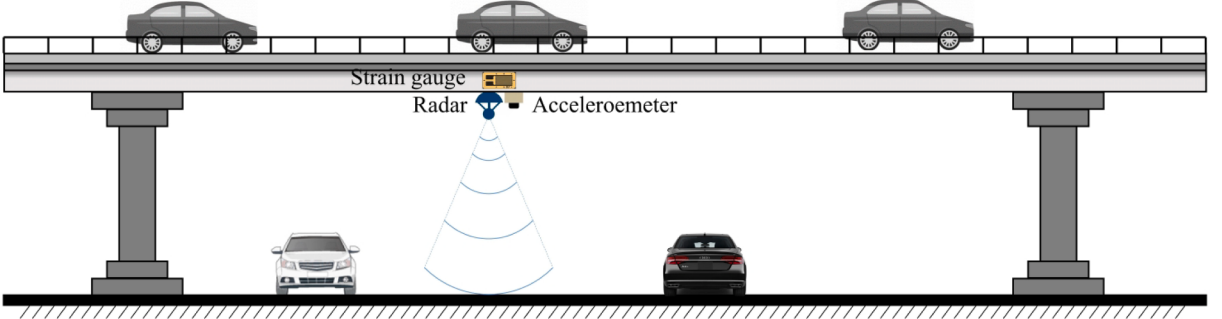
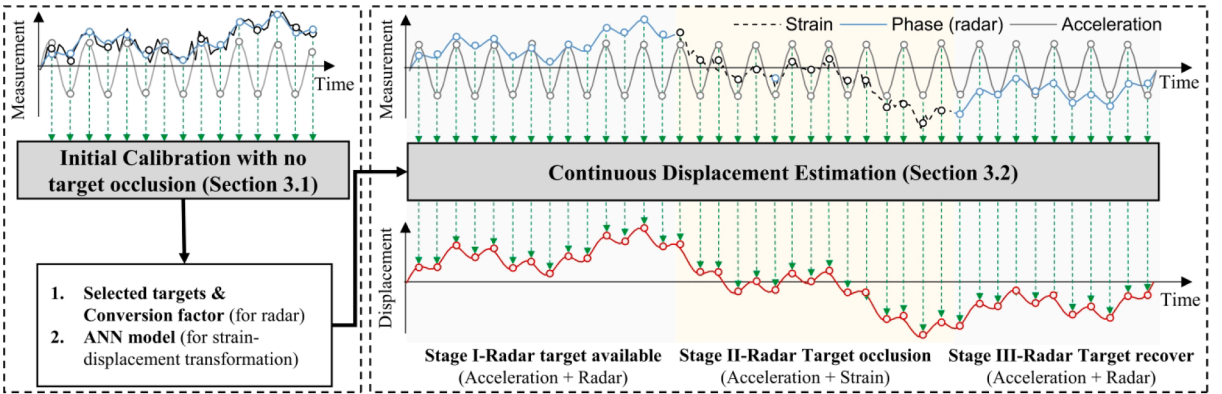


Fig. 1. Drift caused in the radar-based displacement induced by target occlusion owing to phase unwrapping failure.



**Fig. 2.** Sensor setup of the proposed bridge displacement estimation technique using millimeter-wave radar, strain gauge, and accelerometer.



**Fig. 3.** Flowchart of the proposed bridge displacement estimation technique using millimeter-wave radar, strain gauge, and accelerometer.

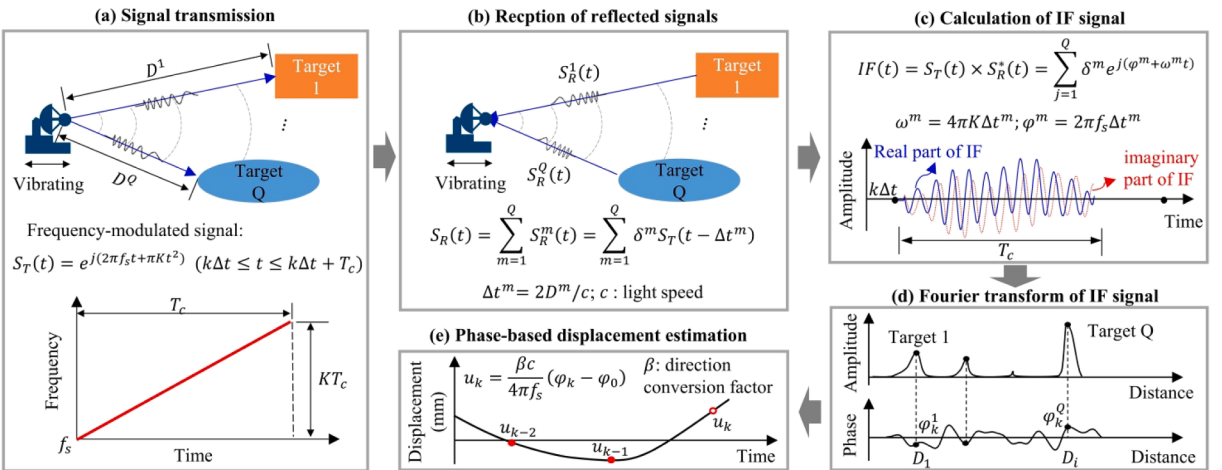


**Fig. 4.** Flowchart of radar-based displacement estimation: (a) transmission of a frequency modulated signal, (b) reception of signal reflected from multiple targets, (c) calculation of an intermediate frequency (IF) signal using transmitted and reflected signals, (d) Fourier transformation of the IF signal, and (e) estimation of displacement using the phase extracted from the selected target.

$$S_R(t) = \sum_{m=1}^Q S_R^m(t) = \sum_{m=1}^Q \delta^m S_T(t - \Delta t^m) = \sum_{m=1}^Q \delta^m \delta^m S_T(t - 2D^m/c) \quad (2)$$

where  $\delta^m$  and  $\Delta t^m$  denote the attenuation factor and traveling time of the  $m^{\text{th}}$  target, respectively;  $D^m$  denotes the distance between the radar and  $m^{\text{th}}$  target, and  $c$  denotes the speed of light.

Next, an intermediate frequency (IF) signal is calculated as,

$$IF(t) = S_T(t) \times S_R^*(t) = \sum_{j=1}^Q \delta^m e^{j(\varphi^m + \omega^m t)}; \omega^m = \frac{4\pi K D^m}{c}; \varphi^m = \frac{4\pi f_s D^m}{c} \quad (3)$$

Note that both the frequency ( $\omega^m$ ) and phase ( $\varphi^m$ ) of the IF signal include the distance information ( $D^m$ ). Subsequently, a Fourier transform is applied to the IF signal, and the peaks in the amplitude spectrum correspond to targets at different distances. Because the radar vibration is insignificant, the phase is commonly adopted to estimate the displacement ( $u$ ) from the selected target [15]:

$$u_k = \frac{\beta c}{4\pi f_s} (\varphi_k - \varphi_0) \quad (4)$$

where  $\varphi_0$  and  $\varphi_k$  denote the initial and current phases extracted from the selected target, respectively. Note that the actual radar vibration direction may differ from the light of sight (LOS) direction, and thus a direction conversion factor ( $\beta$ ) is included in Equation (4).

Radar are not affected by weather or light conditions, and extensive studies have been conducted on radar-based structural displacement estimation over the last two decades. For example, centimeter wave radars with a radio frequency (RF) within 30 GHz have been used to monitor displacements of long-span bridges [15], mid-rise buildings [30], traffic light structures [31], etc. For bridge displacement estimation, a radar is installed at a stationary location (e.g., the pier of a target bridge), and the multi-point displacements of a target bridge are estimated. However, there is no guarantee that a stable reflection could be secured from the desired displacement estimation location of the bridge. In such a case, an artificial reflector needs to be placed at the displacement estimation location, requiring additional effort. In addition, to select a target near the desired displacement estimation location and then estimate the conversion factor ( $\beta$ ) for the selected target, the locations of all the radar-detected targets on the bridge should be manually identified, which is cumbersome. In addition, when the bridge displacement exceeds the radar wavelength, phase wrapping could be a major issue, especially for millimeter-wave radars. Moreover, securing a stationary installation location may not be possible, especially for long-term continuous displacement monitoring. A few attempts have been made to install a radar on a target bridge [32,33] to eliminate the need for a stationary installation location, but they required the installation of an active transponder at a stationary location, which would be cumbersome in practice. Note that all these studies focused on short-period bridge displacement estimation and did not consider potential radar target occlusion, which is common in long-term continuous bridge displacement monitoring.

## 2.2. Strain-based bridge displacement estimation

**Fig. 5** shows an overview of the mode-superposition algorithm for the strain-based displacement estimation. According to the Euler–Bernoulli beam theory, multiple strain measurements along a bridge ( $\varepsilon(x_i, t)$ ,  $i = 1, \dots, N$ ) can be transformed into the displacement at any desired location ( $u(x_d, t)$ ) [9]:

$$u(x_d, t) = \frac{1}{y_c} \Psi(x_d) (\Phi(x)^T \Phi(x))^{-1} \Phi(x)^T \varepsilon(x, t) \quad (5)$$

$$\Psi = [\varphi_1(x_d) \dots \varphi_L(x_d)]_{1 \times N}; \Phi = \begin{bmatrix} \phi_1(x_1) & \dots & \phi_N(x_1) \\ \vdots & \ddots & \vdots \\ \phi_1(x_N) & \dots & \phi_N(x_N) \end{bmatrix}_{N \times N} \quad (6)$$

where  $y_c$  is the vertical distance from the strain sensing location to the neutral axis;  $\varphi_j$  and  $\phi_j$  represent the  $j^{\text{th}}$  displacement and strain mode shape, respectively. However, there are the following limitations: (1) modal shapes and the neutral axis location of the target structure may not be readily available in practice, which causes difficulties in the application of this algorithm; (2) simultaneous data collection at several locations is not convenient; and (3) strain sensors have relatively high noise levels, which deteriorate the accuracy of displacement estimation.

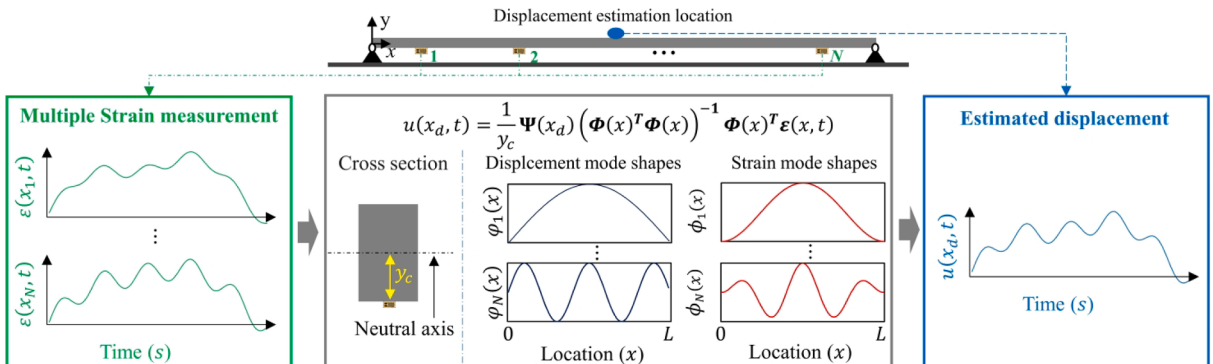


**Fig. 5.** Overview of strain-based displacement estimation using the mode superposition algorithm.

### 2.3. Improved displacement estimation through finite impulse response filter fusion of acceleration and displacement measurements

Considering that the displacement estimated from single sensors may have low accuracy, FIR filters have been used to fuse acceleration and initial displacement measurements [25,34,35] for improved displacement estimation. Fig. 6 presents a flowchart of the FIR filter-based structural displacement estimation techniques. Basically, a high-frequency displacement is first estimated from acceleration measurements using double integration and high-pass filtering, and a low-frequency displacement is estimated from the initial displacement estimation through other sensors, such as strain gauges or vision cameras, using low-pass filtering. The final displacement is then estimated by combining the low- and high-frequency displacements. Assuming that the acceleration-based displacement has a higher accuracy than the initial estimated displacement in the high-frequency band, the final estimated displacement has a better accuracy than the initial estimated displacement. Note that the low- and high-pass filters employed here are complementary, and the cutoff frequency of the filters is determined as the first natural frequency of the target structure [25] or based on the noise characteristics of acceleration and displacement measurements [34].

Previously, attempts have been made to fuse millimeter-wave radar and accelerometers, and some of the limitations of using millimeter-wave radar have been addressed [27]. However, this technique does not work well with intermittent occlusions of radar target. Attempts have also been made to fuse strain gauges and accelerometers, but these techniques require multiple strain sensors and high similarity between the mode shapes of the target structure and a simply supported beam [25,35].

## 3. Development of structural displacement estimation technique by fusing radar, vision camera, and accelerometer

For the bridges shown in Fig. 2, the road under the bridge acts as a target for the millimeter-wave radar, but moving objects such as vehicles may cover these targets. By fusing measurements from collocated millimeter-wave radar, accelerometer, and strain gauge, a continuous displacement estimation technique is proposed for bridge structures that considers intermittent target occlusions. Because the radar is installed at the displacement estimation location, multiple targets with stable reflection will be available within the field of view of the radar. The collocated installation of the radar, accelerometer, and strain gauge on the structure allows for the fusion of three sensors, and offers following additional benefits: (1) automatic selection of the best target required for radar-based displacement estimation and automatic estimation of the conversion factor, (2) adaptive phase unwrapping with the help of acceleration and strain measurements, and (3) continuous displacement estimation even with intermittent radar target occlusion. As shown in Fig. 3, the proposed technique consists of two steps: (1) automated initial calibration (Section 3.1), and (2) continuous displacement estimation (Section 3.2).

### 3.1. Automated initial calibration

Because the millimeter-wave radar is installed at the displacement estimation location of the target bridge, as shown in Fig. 2, multiple targets are usually available within the field of view of the radar, which are detected by the radar; targets with a stable reflection should be selected for bridge displacement estimation. In addition, the radar measures the displacement in the LOS direction, and a direction conversion factor is required to convert the estimated displacement from the LOS direction to actual vibration direction. To estimate the displacement from the strain and acceleration measurements, the strain measurements should be transformed into displacements. Therefore, an ANN model is introduced here for the strain–displacement transformation. An automated initial calibration algorithm is proposed to (1) select good targets and estimate their conversion factors for the radar (Section 3.1.1) and (2) train an ANN model for strain–displacement transformation (Section 3.1.2), assuming that initial measurements from the millimeter-wave radar, strain gauge, and accelerometer are recorded for a short period without any target occlusion.

#### 3.1.1. Automated target selection and conversion factor estimation for the radar

Target selection and conversion factor estimation are accomplished by minimizing the error between the high-frequency radar-based and acceleration-based displacements. The detailed procedure is illustrated in Fig. 7; the first target, i.e., the nearest target, was first selected, and the initial conversion factor was set to 0.5. Two high-frequency displacements were estimated from radar and acceleration measurements, and the root mean square error (RMSE) between them was calculated. Subsequently, by varying the

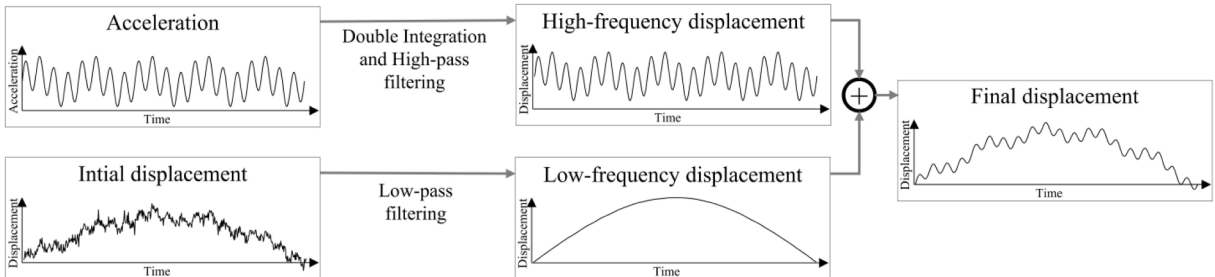


**Fig. 6.** Overview of the improved displacement estimation through the FIR filter fusion of acceleration and initial displacement measurements.

conversion factor value from 0.5 to 2 and repeating the RMSE calculation, the RMSE vs. conversion factor curve was obtained. The final conversion factor was estimated as the value corresponding to the smallest RMSE ( $E$ ). Finally,  $E$  values and conversion factors were obtained for all targets by repeating the previous steps, and multiple targets with small  $E$  values were selected for continuous displacement estimation. Note that the selected targets were ranked by their  $E$  values, and targets with small  $E$  values were preferred for displacement estimation.

### 3.1.2. Fully-automated ANN training for strain–displacement transformation

After target selection and conversion factor estimation, the radar-based displacement was estimated from the best target. Fig. 8 shows an overview of the ANN training for the strain–displacement transformation. Note that both the radar-based displacement and strain measurement are low-pass filtered before training the ANN model. The necessity of low-pass filtering can be justified based on the following: (1) strain measurement usually has a low signal-to-noise ratio (SNR), and low-pass filtering can significantly improve the SNR; and (2) strain measurement only contributes to low-frequency displacement estimation in continuous displacement estimation (Section 3.2). Finally, an ANN model was trained to transform low-frequency strain to low-frequency displacement. Training was performed in MATLAB using the Neural Network Toolbox, and hyperparameters, such as the number of hidden layers and delayed steps, were optimized using cross-validation. Note that the ANN model has been extensively used in the existing literature [36,37]; thus, the principle of ANN and detailed procedure for ANN training are omitted here.

## 3.2. Continuous bridge displacement estimation

After the initial calibration, the displacement was estimated continuously. Depending on whether the selected targets are occluded, all time steps can be categorized into three stages; the displacement estimation procedure for each stage is explained below.

### 3.2.1. Stage I: Radar target available

At this stage, at least one of the selected radar targets was not occluded, and the displacement could be estimated using millimeter-wave radar and accelerometer measurements. Fig. 9 shows a flowchart of the displacement estimation in Stage I. Displacement was first estimated from radar measurements. Owing to the phase wrapping issue, an acceleration-aided adaptive phase unwrapping algorithm is applied here [27]. Subsequently, a low-frequency displacement was estimated from the radar-based displacement, and a high-frequency displacement was estimated from the acceleration measurement. The final displacement was estimated by combining the low- and high-frequency displacements, which had a better accuracy than the radar-based displacement. Additional details on displacement estimation using millimeter-wave radar and accelerometer measurements can be found in Ma et al. [27].

As explained in Section 3.1.1, multiple targets were selected and ranked for the millimeter-wave radar. Subsequently, the best target was first used, and when the best target is occluded, other targets were used. A key issue here is the automatic detection of target occlusion. As shown in Fig. 10, at each time step, an amplitude spectrum can be obtained by applying a Fourier transform to the IF signal (Fig. 4(d)). The target occlusion causes a change in the amplitude spectrum around the target. Therefore, a target spectrum can be defined as the spectrum in the range  $[D - \Delta D, D + \Delta D]$ , as shown in Fig. 10; a similarity score can be calculated between the target spectra in the first and current time steps ( $F_1(d)$  and  $F_i(d)$ ,  $D - \Delta D \leq d \leq D + \Delta D$ ). Here, the best target at a distance of  $D$  is used as an example, and target occlusion detection is applied for all selected targets. A similarity score other than one indicates occlusion of the target. However, the bridge vibration causes a change in the distance between the radar and target, which is reflected by a minor shift along the  $x$ -axis (i.e., distance axis) in the amplitude spectrum. The spectral shift also triggers a change in the similarity score, causing difficulty in target occlusion detection.

Fig. 11 shows a flowchart of the proposed target occlusion detection algorithm, which is robust to bridge vibrations. Spline interpolation was first applied to the target spectra at the first and current time steps to obtain high-sampled target spectra ( $(F_{1,H}(d)$  and  $F_{i,H}(d)$ ,  $D - \Delta D \leq d \leq D + \Delta D$ ). The spectral shift ( $\Delta d$ ) induced by bridge vibration can be estimated by calculating their correlation coefficients, and the current target spectrum is shifted by  $\Delta d$  to obtain synchronized target spectra ( $F_{1,H}(d)$  and  $F_{i,H}(d + \Delta d)$ ,

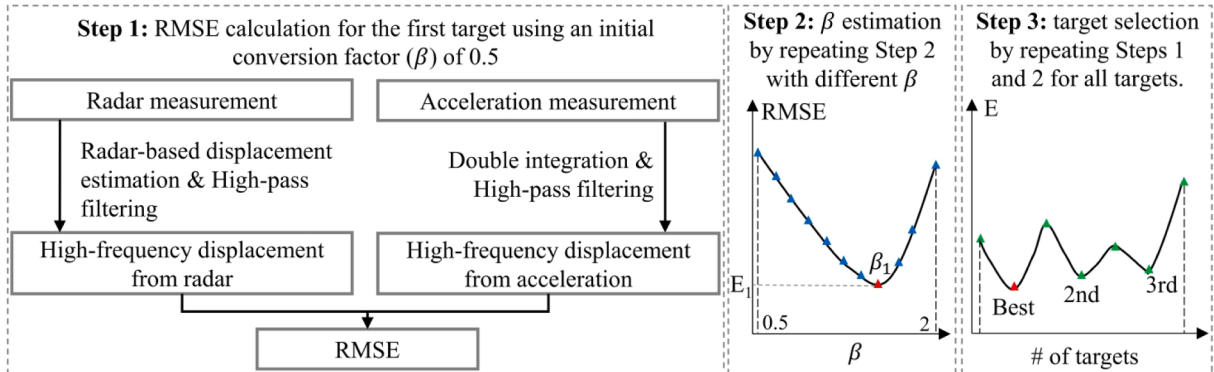


Fig. 7. Automated target selection and conversion factor estimation.

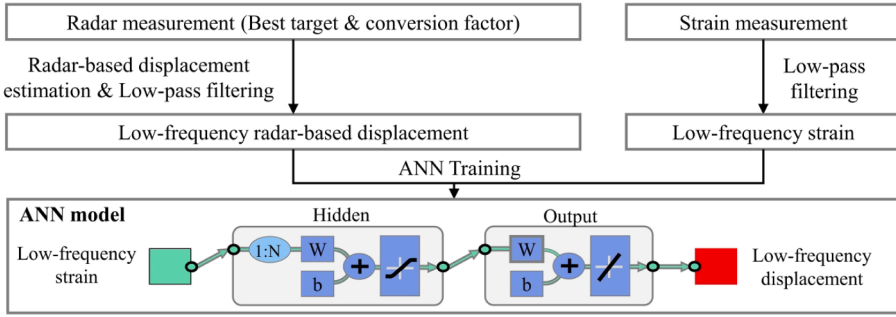


Fig. 8. Overview of ANN training for strain–displacement transformation.

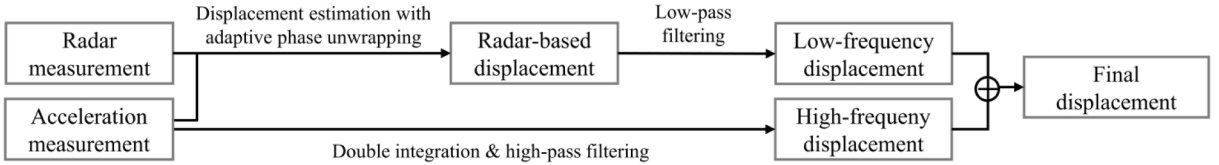


Fig. 9. Flowchart of displacement estimation using radar and acceleration measurements in Stage I.

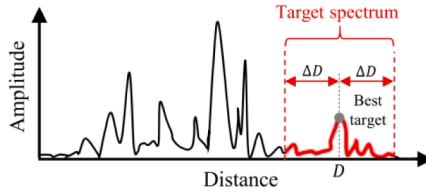


Fig. 10. Target spectrum defined for detecting the occlusion of the best target.

$D - \Delta D \leq d \leq D + \Delta D$ ). Considering the low distance resolution of the target spectrum and small bridge displacement, spline interpolation is necessary. Finally, a similarity score is calculated from the synchronized target spectra as

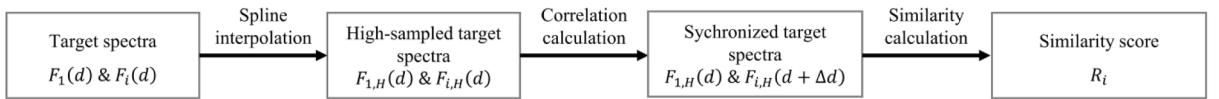
$$R = \frac{\sum_{|d-D| \leq \Delta D} F_{1,H}(d) F_{i,H}(d + \Delta d)}{\sqrt{\sum_{|d-D| \leq \Delta D} \{F_{1,H}(d)\}^2 \{F_{i,H}(d + \Delta d)\}^2}} \quad (7)$$

The calculated similar score is usually noisy and, therefore, smoothed using a moving average filter. Here, a threshold of the similarity score ( $R_T$ ) is required for target occlusion detection, and its value is determined as

$$R_T = \bar{R} - 3\sigma_R \quad (8)$$

where  $\bar{R}$  and  $\sigma_R$  denote the mean and standard derivation of the similarity scores calculated from the radar measurements used for the initial calibration. Other algorithms, such as Zoom FFT [38] and Chirp Z-Transform [39], can also be applied here to obtain a high-sampled spectral; however, they are not significantly different than spline interpolation. Therefore, spline interpolation is used here because of its simplicity in the algorithm implementation.

As described in Section 3.1.1, multiple targets are selected and ranked by their E-values. Following the flowchart above, at each time step, a similarity score is calculated for each of these selected targets. The best target is initially used for radar-based displacement estimation. If its similarity score is less than the threshold value, meaning that the best target is occluded, then the 2nd target is used for displacement estimation. This process continues until all targets are occluded.



Note: Subscripts 1 and  $i$  denote the 1<sup>st</sup> and  $i$ <sup>th</sup> time step, respectively;  $\Delta d$  denotes spectral shift caused by bridge vibration.

Fig. 11. Flowchart of the proposed target occlusion detection algorithm.

### 3.2.2. Stage II: Radar target occlusion

Once  $R$  is smaller than  $R_T$  for all targets selected from the millimeter-wave radar, displacement is estimated using a strain gauge and accelerometer, both of which can be used for displacement estimation without the need for any target. Fig. 12 shows a flowchart of the displacement estimation using the strain and acceleration measurements in Stage II. The strain measurement was first low-pass filtered and then transformed into low-frequency displacement using the trained ANN model. In contrast, high-frequency displacement is estimated from acceleration measurements by double integration and high-pass filtering. The final displacement was estimated by combining low- and high-frequency displacements. During the target occlusion, the millimeter-wave radar is still running, and the amplitude spectrum extracted from the radar measurement is used for target occlusion detection.

However, changes in ambient temperature, self-heating of the strain gauges, and other factors may introduce zero drift in the strain measurement [28], resulting in a bias in the estimated displacement. Fig. 13 shows the removal of this potential displacement bias. Two displacements ( $u_{k-1}^{r+a}$  and  $u_{k-1}^{s+a}$ ) at the last time step of Stage I (e.g.,  $(k-1)^{th}$  time step) can be estimated using radar and acceleration measurements and strain and acceleration measurements, respectively. The bias can be estimated as the difference between two displacements.

$$Bias = u_{k-1}^{s+a} - u_{k-1}^{r+a} \quad (9)$$

Note that, displacement differences can be estimated for the last several time steps of Stage I, and the averaged displacement difference can be used as a bias to improve the robustness of the bias estimation. The final displacement at Stage II can be estimated by removing this bias from the displacement estimated using the acceleration and strain measurements.

$$u_k^f = u_k^{s+a} - Bias = u_k^{s+a} - u_{k-1}^{s+a} + u_{k-1}^{r+a} = u_k^{s+a} - u_{k-1}^{s+a} + u_{k-1}^f \quad (10)$$

Here, the zero-drift of the strain measurement is assumed to be constant in the last time steps and in stage II. This assumption is reasonable considering that the target occlusion period is typically only several seconds to a few minutes.

### 3.2.3. Stage III: Radar target recover

With  $R$  larger than  $R_T$  for at least one selected radar target, the displacement was estimated again using a millimeter-wave radar and accelerometer. However, the acceleration-aided adaptive phase-unwrapping algorithm cannot work because the phase at the last two time steps of stage II is not available. To address this issue, the displacement is still estimated at the first two time steps of stage III using strain and acceleration measurements, and the estimated displacement is used to recover the unwrapped phase at these two steps (as shown in Fig. 14). For the following stages of stage III, the acceleration-aided adaptive phase-unwrapping algorithm [27] can be applied without the need for strain measurement. The displacement estimation in this stage is exactly the same as that in Stage I; therefore, the details are not repeatedly provided given here.

## 4. Laboratory test on a 10-m-long beam-type structure

### 4.1. Experimental setup

To validate the performance of the proposed technique, a laboratory test was conducted on a 10-m-long beam-type structure, as shown in Fig. 15(a). The structure was supported at its two ends to simulate hinge connection. Fig. 15(b) shows the overall setup of the 10-m-long beam-type structure test. A TI IWR1642 millimeter-wave radar (Fig. 15(c)), PCB Piezotronics 3713B112G MEMS-type accelerometer (Fig. 15(d)), and TML FLA-1-11-1LJC resistance-type strain gauge (Fig. 15(e)) were installed approximately at 1/2 span for displacement estimation. The detailed specifications of the sensors are listed in Table 1. Polytech RSV-150 LDV (Fig. 15(f)) is used to measure reference displacement, which evaluates the displacement estimation performance of the proposed technique. All acceleration, strain, and LDV measurements were sampled at 100 Hz using a National Instruments data-acquisition device. The millimeter-wave radar transmits a frequency-modulated signal with a duration of 60  $\mu$ s, frequency slope of 64.985 MHz/ $\mu$ s, and time interval of 0.01 s. To fully validate the proposed technique, a total of nine cases were considered in this test, as shown in Table 2. During the test, the structure had millimeter-level vibrations generated by a researcher jumping or walking on the structure.

### 4.2. Initial calibration results

The strain gauge, millimeter-wave radar, and accelerometer measurements in Case 1 were used for the initial calibration. The targets detected by the radar are shown in Fig. 16. Note that this test mainly validates the possibility of switching between the fusion of

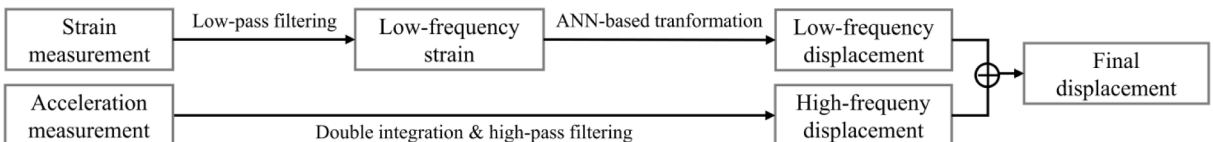
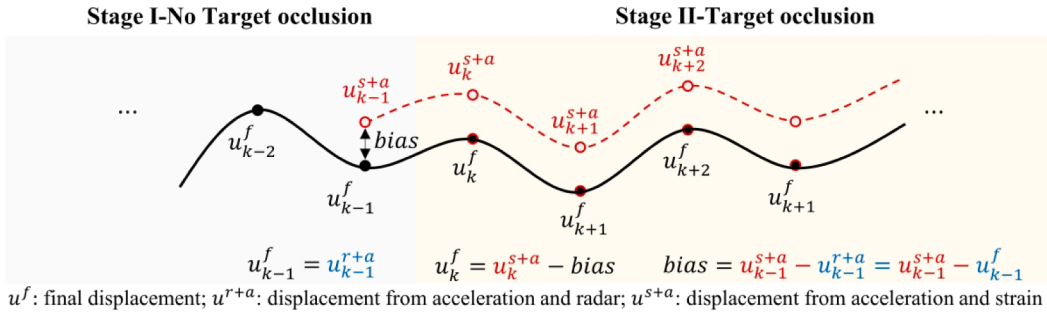
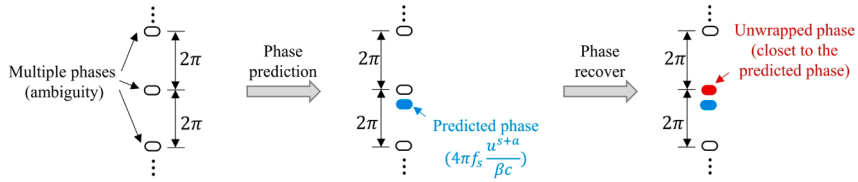


Fig. 12. Displacement estimation using strain and acceleration measurements during radar target occlusion.



**Fig. 13.** Removal of potential bias in displacement estimated using strain and acceleration measurements induced using strain and acceleration measurements induced by zero-drift of strain measurement.



**Fig. 14.** Phase unwrapping at first two time steps of stage III using displacement estimated from strain and acceleration measurements.

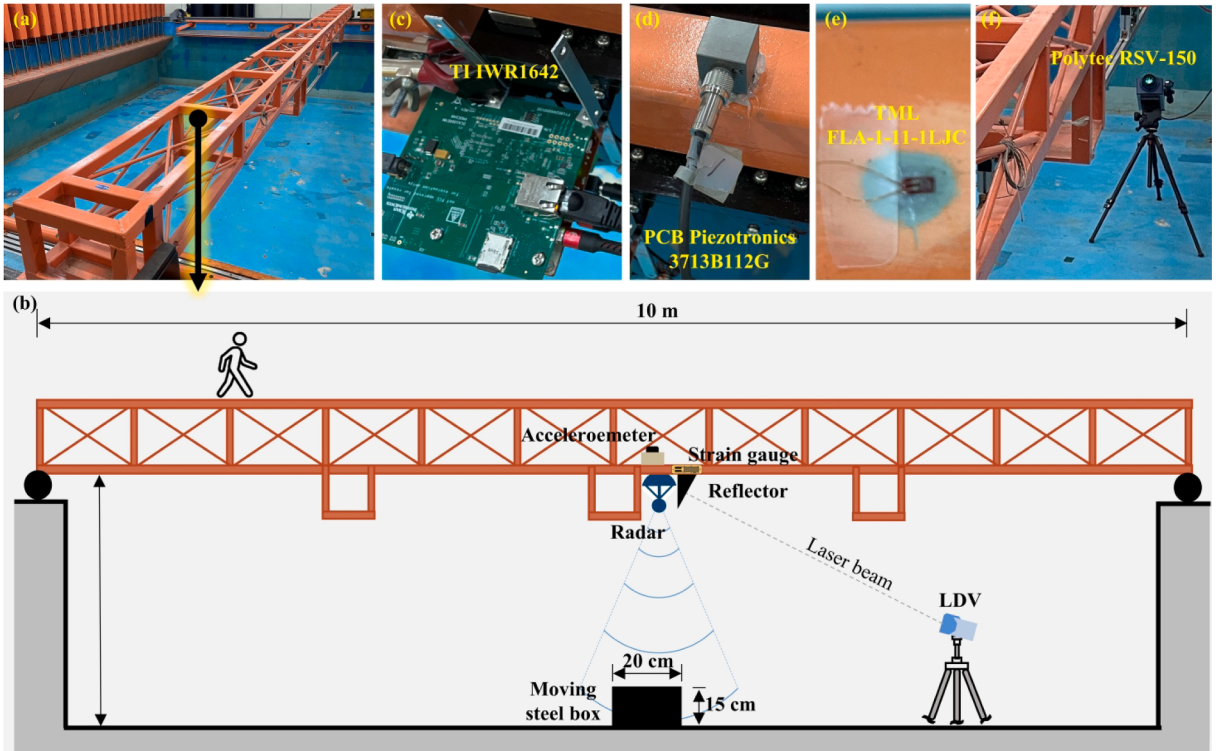


**Fig. 15.** Laboratory test on a 10-m-long beam-type structure: (a) overview of the structure, (b) overall experimental setup, (c) TI IWR1642 millimeter-wave radar, (d) PCB MEMS accelerometer, and (e) FLJ-10-111 resistance-type strain gauge installed approximately at 1/2 span for displacement estimation, and (f) Polytech RSV-150 LDV for ground-truth displacement measurement.

radar and acceleration and that of strain and acceleration. For the fusion of radar and acceleration, the best target selected at a distance of 2.27 m was used, and its conversion factor was estimated to be 0.986. The switching between different targets for the radar is validated in Section 5.

**Table 1**

Detailed specifications of accelerometer, strain gauge, and millimeter-wave radar used in the 10-m-long beam-type structure test.

Sensors	Parameters	Values
Accelerometers (PCB Piezotronics 3713B112G)	Bandwidth	DC – 250 Hz
	Full-scale range	$\pm 2g$
	Operating temperature	-54 ~ 121 °C
	Sensitivity	1,000 mV/g
	Spectral noise	22.9 $\mu\text{g}/\sqrt{\text{Hz}}$
	Linearity	<1%
Strain gauges (TML FLA-1-11-1LJC)	Grid material	Cu-Ni alloy
	Gauge factor	$2.10 \pm 1\%$
	Gauge resistance	$120 \pm 0.5 \Omega$
	Operating temperature	-20 ~ 80 °C
	Transverse sensitivity	-0.5%
	Starting frequency	77 GHz
Millimeter-wave radar (TI IWR1642)	Bandwidth	Up to 4 GHz
	Transmit power	12.5 dBm
	RX Noise Figure	15 dB
	Phase Noise at 1 MHz	-93 dBc/Hz
	Operating temperature	-40 ~ 105 °C

**Table 2**

Descriptions of nine cases in the 10-m-long beam-type structure test.

# of cases	Test duration (s)	Intermittent target occlusion	Artificial temperature variation	Purposes
1	90	No	No	Initial calibration
2	90	No	No	The performance of displacement estimation using strain gauge and accelerometer
3				
4	90	Yes	No	The robustness of the proposed technique to intermittent target occlusion
5				
6				
7	90	No	Yes	The robustness of the proposed technique to environmental temperature variation
8				
9	4500	No	No	The robustness of the proposed technique for long-term continuous monitoring

The displacement estimated from the best target is used as the ground-truth displacement to train an ANN model for the strain–displacement transformation. Fig. 17 shows the radar-based displacement estimation process. The raw phase constrained in the range  $[-\pi, \pi]$  (Fig. 17(a)) was successfully recovered by the acceleration-aided adaptive phase unwrapping algorithm (Fig. 17(b)). Therefore, displacement is estimated from radar measurements with an RMSE of 0.059 mm (Fig. 17(c)), which is sufficiently accurate to act as the ground-truth value for ANN training.

Here, low-frequency strain and radar-based displacement were utilized as the input and output of the ANN model, respectively. The cutoff frequency of the low-pass filter was set to 1 Hz; Fig. 18 shows the ANN architecture. The delay was set to five, and the number of hidden layers was also set to five after trial and error. With a test duration of 90 s and sampling rate of 100 Hz, a total of 9000 data points was available. These data points were randomly divided into three parts: 50% were used for training, 25% for validation, and 25% for testing. The Levenberg–Marquardt algorithm was selected for training, and the mean squared error (MSE), which is a commonly used indicator of training results, was utilized. The displacements estimated using the strain and acceleration measurements using the trained ANN model and FIR filter are shown in Fig. 17(c), and the RMSE of the estimated displacement is only 0.091 mm.

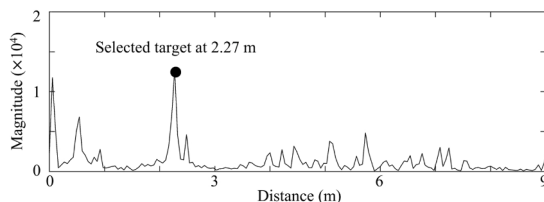
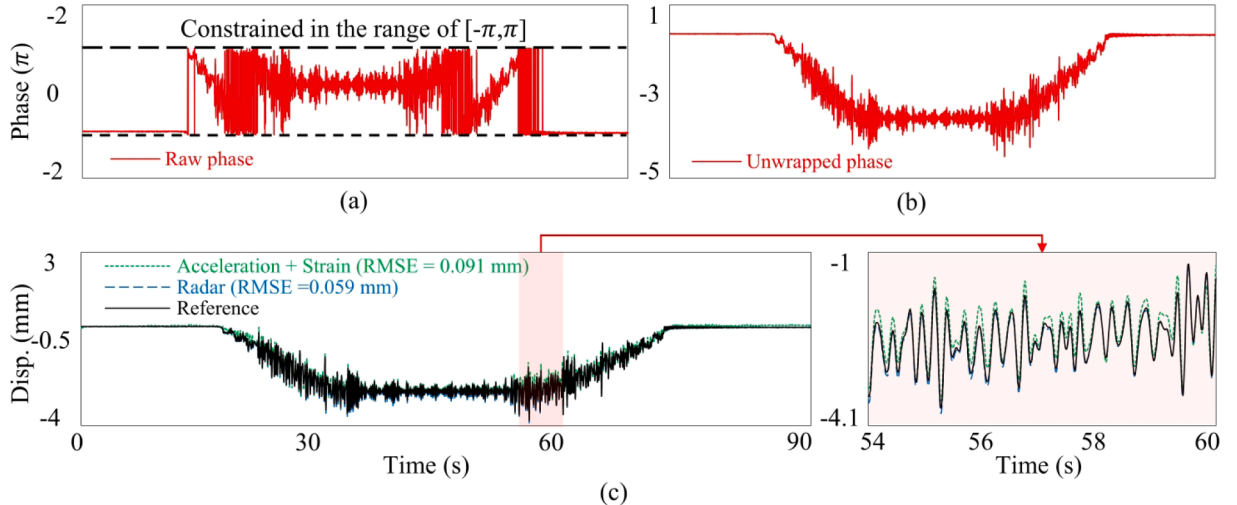
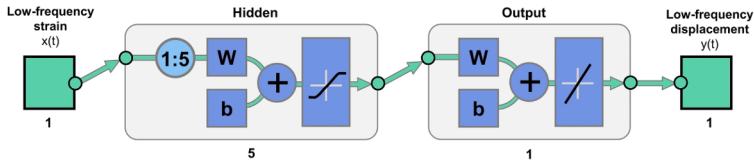


Fig. 16. Target detection result.



**Fig. 17.** Displacement estimation result for case 1: (a) raw phase extracted from radar measurement, (b) unwrapped phase using acceleration measurement, and (c) estimated displacements.



**Fig. 18.** ANN architecture used for strain-displacement transformation.

#### 4.3. Displacement estimation results

##### 4.3.1. Displacement estimation without target occlusion or artificial temperature variation (cases 1–3)

Fig. 19 shows the displacement estimation results for cases 2 and 3 without target occlusion and temperature variation. Although displacements estimated from strain and acceleration measurements have a little higher error compared to those estimated by the proposed technique, RMSEs are below 0.1 mm. This indicates that displacements can be accurately estimated from collocated strain and acceleration measurements with the trained ANN model and FIR filters. Note that without radar target occlusion, displacements estimated by the proposed technique are identical to those estimated using radar and accelerometer.

In addition, the RMSEs of the displacements estimated from the strain and acceleration measurements using a combination of ANN and FIR filters and the existing technique [25] are compared in Table 3. The existing technique transforms the full-band strain to full-band displacement using the mode superposition algorithm (MSA) explained in Section 2.2; subsequently, it fuses the strain-based displacement with the acceleration using FIR filters. A superior performance is achieved by the combination of ANN and FIR filters, and an average of 58% of the errors is reduced. Note that MSA in the existing technique requires multiple distributed strain gauges and, therefore, has poor performance when a single strain gauge is used [25].

The proposed radar target occlusion detection algorithm was also applied to radar measurements, and the results are shown in Fig. 20. A strong reflection was stably observed from the selected target (Fig. 20(a)), and the similarity score was always close to one in

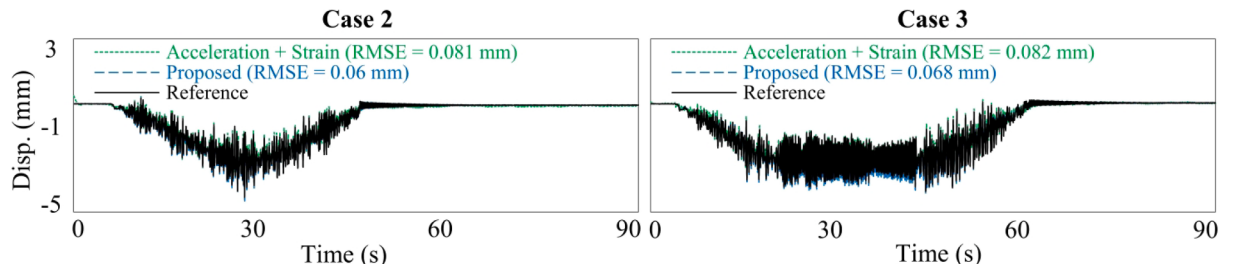


**Fig. 19.** Displacement estimation results without temperature variation and target occlusion in the test of 10-m-long beam-type structure (Cases 2 and 3).

**Table 3**

RMSEs of displacements estimated from strain and acceleration measurements using different techniques in the 10-m-long beam-type structure test (Cases 1 ~ 3).

# of cases	MSA + FIR (mm) [25]	ANN + FIR (mm)	Improvement
1	0.224	0.091	59.38%
2	0.146	0.081	44.52%
3	0.232	0.082	64.66%
Average	0.201	0.085	57.71%

all three cases (Fig. 20(b)); this was consistent with the fact that the best target was not occluded in these tests. Note that the similarity score estimated using Equation (8) was relatively noisy, and a moving average filter of the order of 101 was applied.

#### 4.3.2. Displacement estimation with intermittent target occlusion (cases 4–6)

Fig. 21 shows radar target occlusion detection results for cases 4–6, where intermittent target occlusion was generated by moving a steel box on the ground. The steel box had a length of 90 cm, width of 20 cm, and height of 15 cm. When the selected target was occluded by the box, strong reflection was obtained from the box instead of the selected target (Fig. 21(a)); accordingly, extremely low similarity was observed during this period (Fig. 21(b)).

Fig. 22 shows displacement estimation results for cases 4–6. Owing to the intermittent target occlusion, huge errors are observed in displacements estimated from radar and acceleration measurements. Note that the intermittent target occlusion causes incorrect displacement during the target occlusion period and a large displacement drift after the target occlusion period. Displacements were accurately estimated using strain and acceleration measurements and the proposed technique. However, better performance is achieved by the proposed technique fusing three sensors, and the displacements were estimated with an error of approximately 0.1 mm.

#### 4.3.3. Displacement estimation with artificial temperature variation (cases 7–8)

Fig. 23 shows displacement estimation results for cases 7–8, where environmental temperature variation was artificially generated using a halogen lamp. Because strain measurements are highly sensitive to temperature variation, large errors are observed in displacements estimated from strain and acceleration measurements. However, the proposed technique estimates displacement accurately with approximately 0.1-mm error. Again, without target occlusion, displacements estimated by the proposed technique are identical to those estimated using radar and accelerometer. Considering that environmental temperature variation is common in practice, using only strain and acceleration measurements for long-term continuous displacement monitoring is not feasible.

#### 4.3.4. Continuous displacement estimation for 75 min (case 9)

Fig. 24 shows displacement estimation results for case 9, where the displacement was continuously estimated for 4500 s. As pointed out by a previous study [28], strain gauge measurement suffers from a low-frequency zero-drift due to the heating by electric current. Thus, a low-frequency drift is observed in the displacement estimated from strain and acceleration measurement. This reiterates that the combination of strain and acceleration measurements does not apply to long-term continuous displacement monitoring. The proposed technique estimates displacement accurately for 4500 s, and the RMSE of the estimated displacement is approximately 0.1 mm.

RMSEs of displacements estimated using strain and acceleration measurements were also calculated for every 15, 45, and 90 s, and

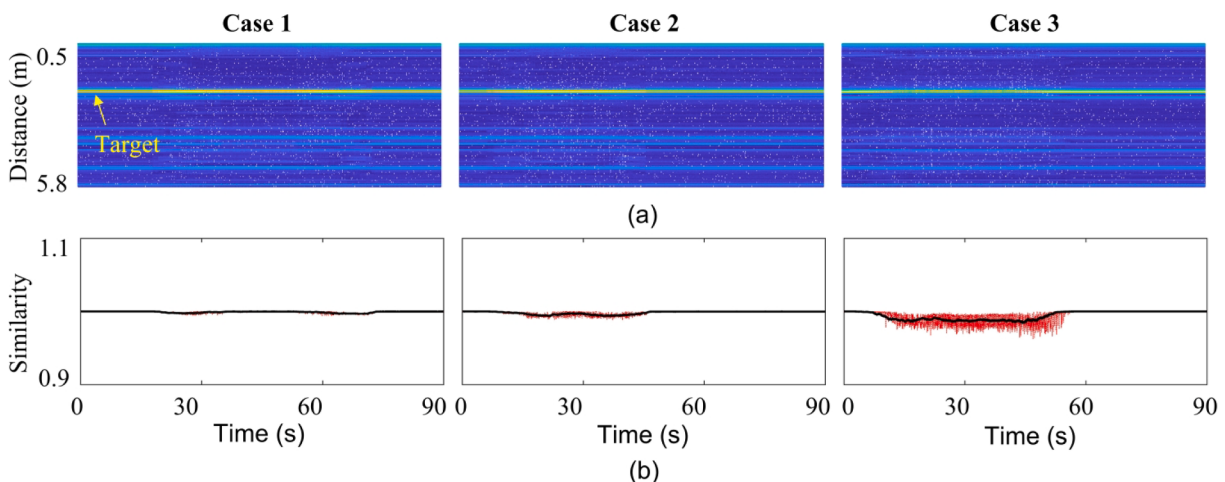
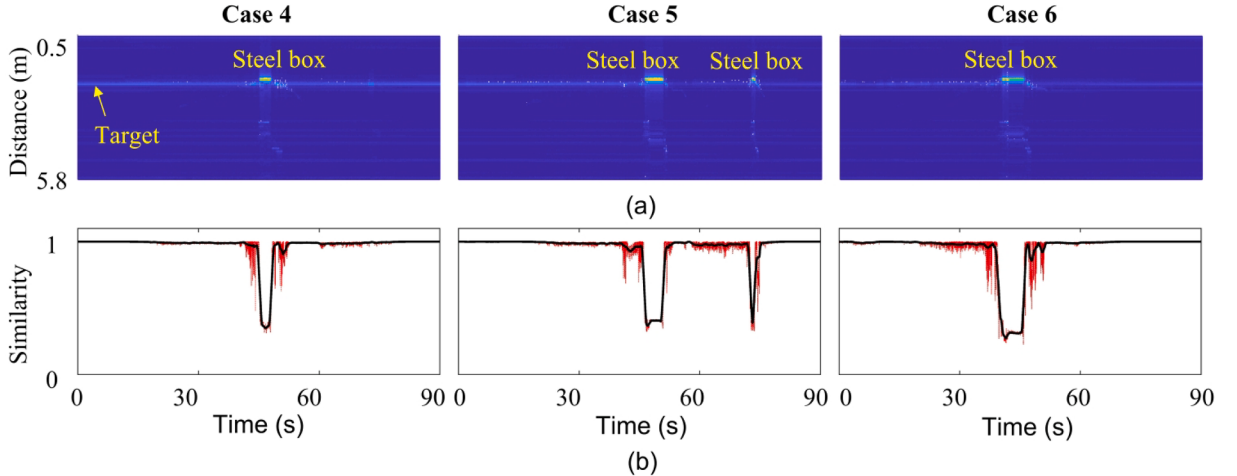
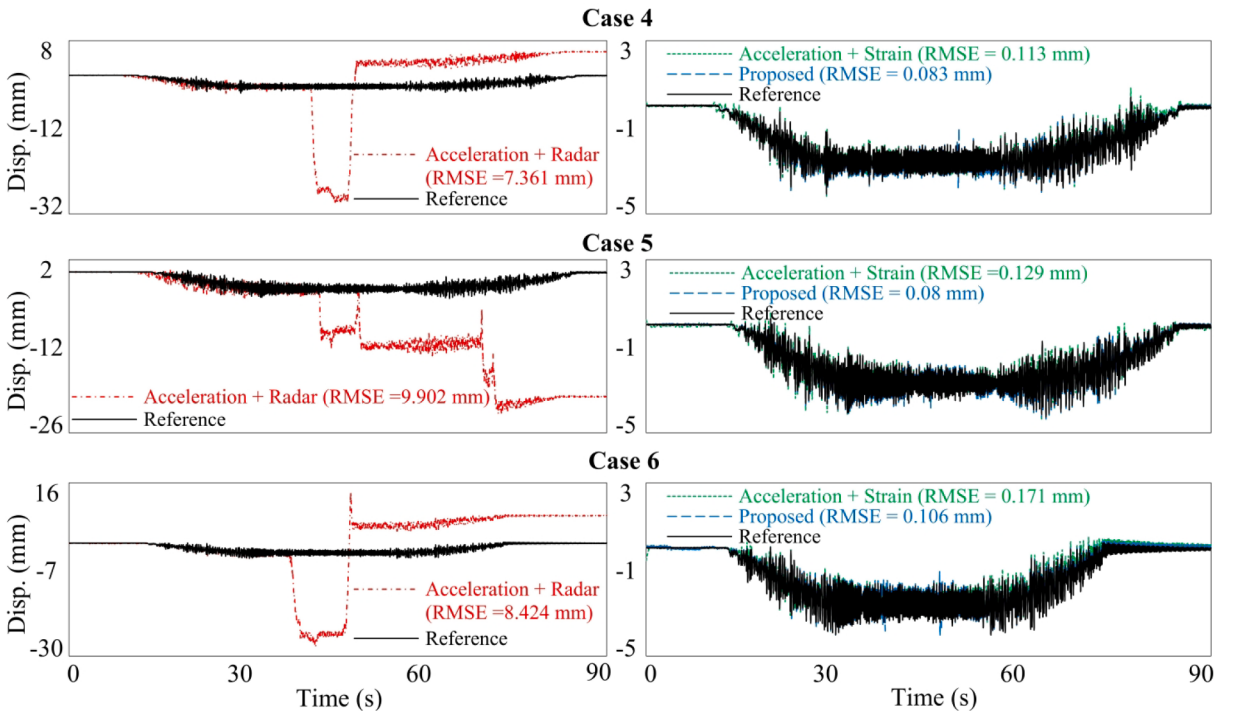


Fig. 20. Target occlusion detection results without intermittent target occlusion in the 10-m-long beam-type structure test (Cases 1–3): (a) amplitude spectrum and (b) similarity scores before and after moving average filtering and detected target occlusion period.



**Fig. 21.** Target occlusion detection results with intermittent target occlusion in the 10-m-long beam-type structure test (Cases 4–6): (a) amplitude spectrum and (b) similarity scores before and after moving average filtering.



**Fig. 22.** Displacement estimation results with intermittent target occlusion in the 10-m-long beam-type structure test (Case 4–6).

the results are shown in Fig. 25. The maximum RMSE of 0.2 mm is acceptable for displacement estimation during the radar target occlusion period. Note that the displacement drifts were removed, as explained in Section 3.2.

#### 4.3.5. Displacement estimation summary for all 9 cases

Table 4 summarizes the RMSEs of the displacements estimated using different sensor combinations for all 9 cases. The proposed technique, which integrates three sensors, is more robust to intermittent target occlusion, environmental temperature variation, and long-term continuous monitoring than the other two combinations. The displacements were always estimated accurately with an overall RMSE of 0.1 mm.

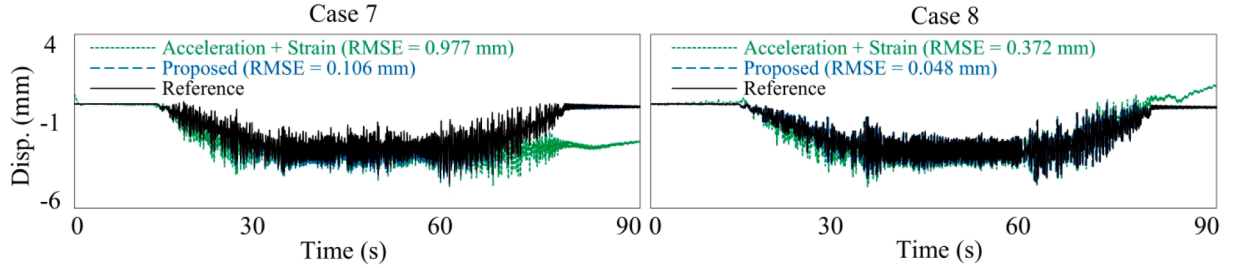


Fig. 23. Displacement estimation results with temperature variation in the 10-m-long beam-type structure test (Cases 7 and 8).

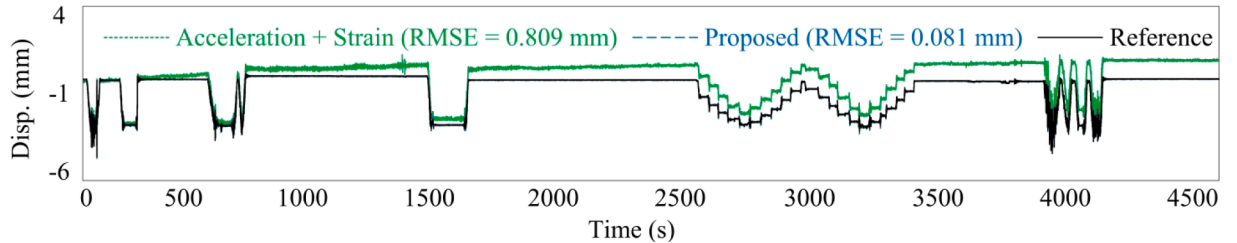


Fig. 24. Displacement estimation results for long-term monitoring in the 10-m-long beam-type structure test (Case 9).

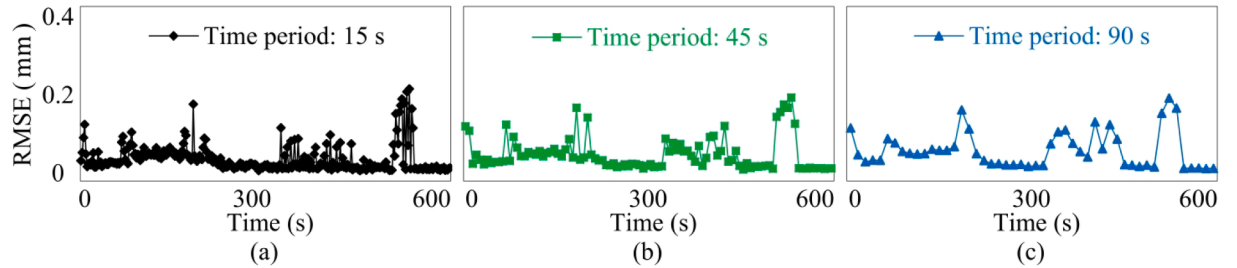


Fig. 25. RMSEs of displacements estimated using strain and acceleration measurements for different short periods: (a) 15 s, (b) 45 s, and (3) 90 s.

Table 4

Summary of RMSEs (mm) of displacements estimated using different sensor combinations.

# of cases	Strain gauge + accelerometer	Millimeter-wave radar and accelerometer	Millimeter-wave radar + strain gauge + accelerometer (Proposed technique)
1	0.091	0.049	0.049
2	0.081	0.06	0.06
3	0.082	0.068	0.068
4	0.113	7.361	0.083
5	0.129	9.902	0.08
6	0.171	8.424	0.106
7	0.977	0.106	0.106
8	0.372	0.048	0.048
9	0.809	0.081	0.081

## 5. Pedestrian steel box-girder bridge test

### 5.1. Experimental setup

The proposed technique was further validated on a steel box-girder pedestrian bridge located in Daejeon, Korea (Fig. 26(a)). The bridge is 45 m long and 8 m wide having a uniform cross section throughout its length. The distance between the top surface of the bridge and ground was approximately 6 m. Fig. 26(b) shows the experimental setup; the millimeter-wave radar, strain gauge, and accelerometer identical to those used in the previous test were installed at half span of the bridge (Fig. 26(c)), where the displacement was estimated. Polytech RSV-150 LDV was installed under the bridge to measure its reference displacement (Fig. 26(d)). The bridge

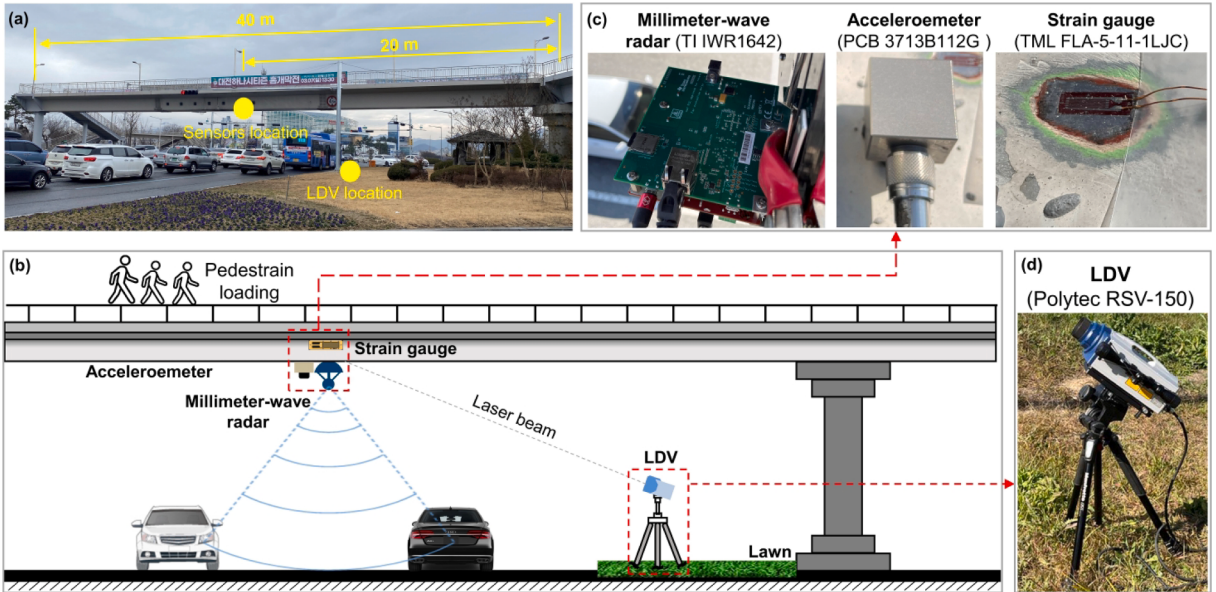


**Fig. 26.** Pedestrian steel box-girder bridge test: (a) overview of the bridge, (b) overview of the experimental setup, (c) an accelerrometer, a strain gauge, and a millimeter-wave radar installed at 1/2 span location for displacement estimation, and (d) LDV for reference displacement measurement.

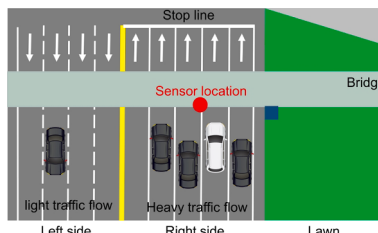
vibration was excited by multiple people slowly passing through the bridge and/or jumping at half span. Other experimental setups were the same as used in the previous laboratory test.

Fig. 27 shows traffic condition of the road under the bridge. The traffic flow was heavy on the right side of the road and light on the left side during the test. In addition, there was a stop line at right side of the road, and the vehicles were stopped under the bridge during red light period. Note that sensor location corresponds to the central area of the right side of the road.

## 5.2. Initial calibration results

The initial calibration requires that no occlusion occurs for the millimeter-wave radar. Therefore, sensor data recordings should begin when there is no traffic on the road. However, the traffic flow was heavy, particularly on the right side of the road during the test period, and it was challenging to continuously obtain radar measurements for a time period (e.g., 1 min) without any radar target occlusion. Therefore, we randomly started sensor data recordings and applied the proposed radar target occlusion detection algorithm to the recorded radar measurement. Based on the radar target detection results, there was no radar target occlusion from 414 s to 419 s, and the data during this period were used for radar target selection and conversion factor estimation. Fig. 28(a) shows the radar target detection results, and the best target (i.e., target 1) was automatically selected at a distance of 6.76 m. The second target (i.e., target 2) was selected at a distance of 9.57 m, which had a small  $E$  value and was relatively far from target 1. Note that several other targets with similar RMSE level were available in the distance range of 7–8 m; however, they were near target 1 and were simultaneously occluded with target 1 considering the relatively large size of the moving vehicles. Fig. 28(b) and (c) show the estimated conversion factors, which are 0.95 and 1.47 for the targets 1 and 2, respectively.

For ANN training, the displacements estimated from target 1 should be used as the ground-truth displacement. However, occlusion occurred frequently for Target 1, and it was challenging to find a sufficiently long time period when Target 1 was not occluded. Therefore, the radar-based displacement estimated from target 2 was used; strain, radar, and acceleration measurements from 170 s to 250 s were used for ANN training. The ANN structure and training parameters were identical to those used in the lab-scale test;



**Fig. 27.** Description of traffic condition during the field test.

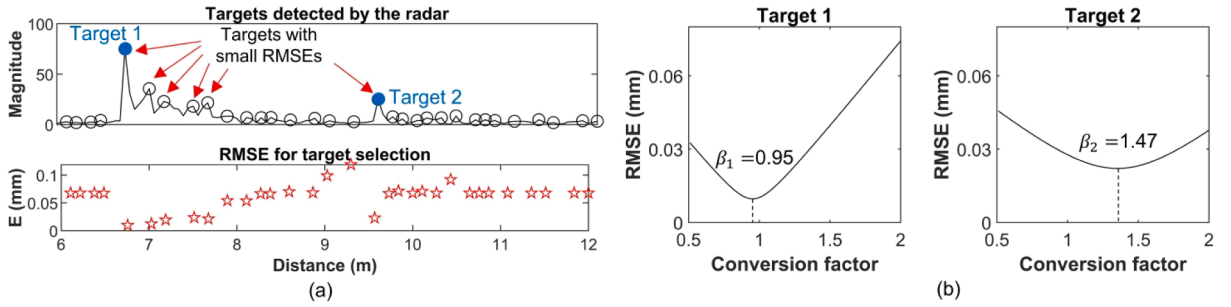


**Fig. 28.** Initial calibration results for millimeter-wave radar: (a) target detection and selection results and (b) conversion factor estimation results for the two selected targets.

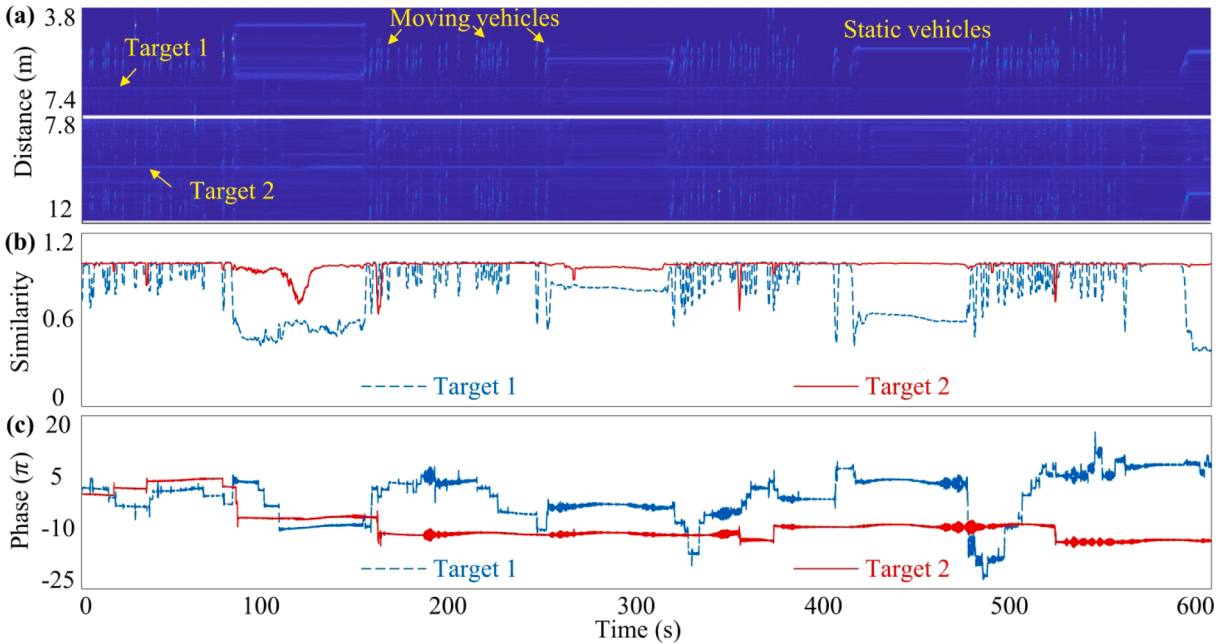
therefore, the details are omitted here.

### 5.3. Displacement estimation results

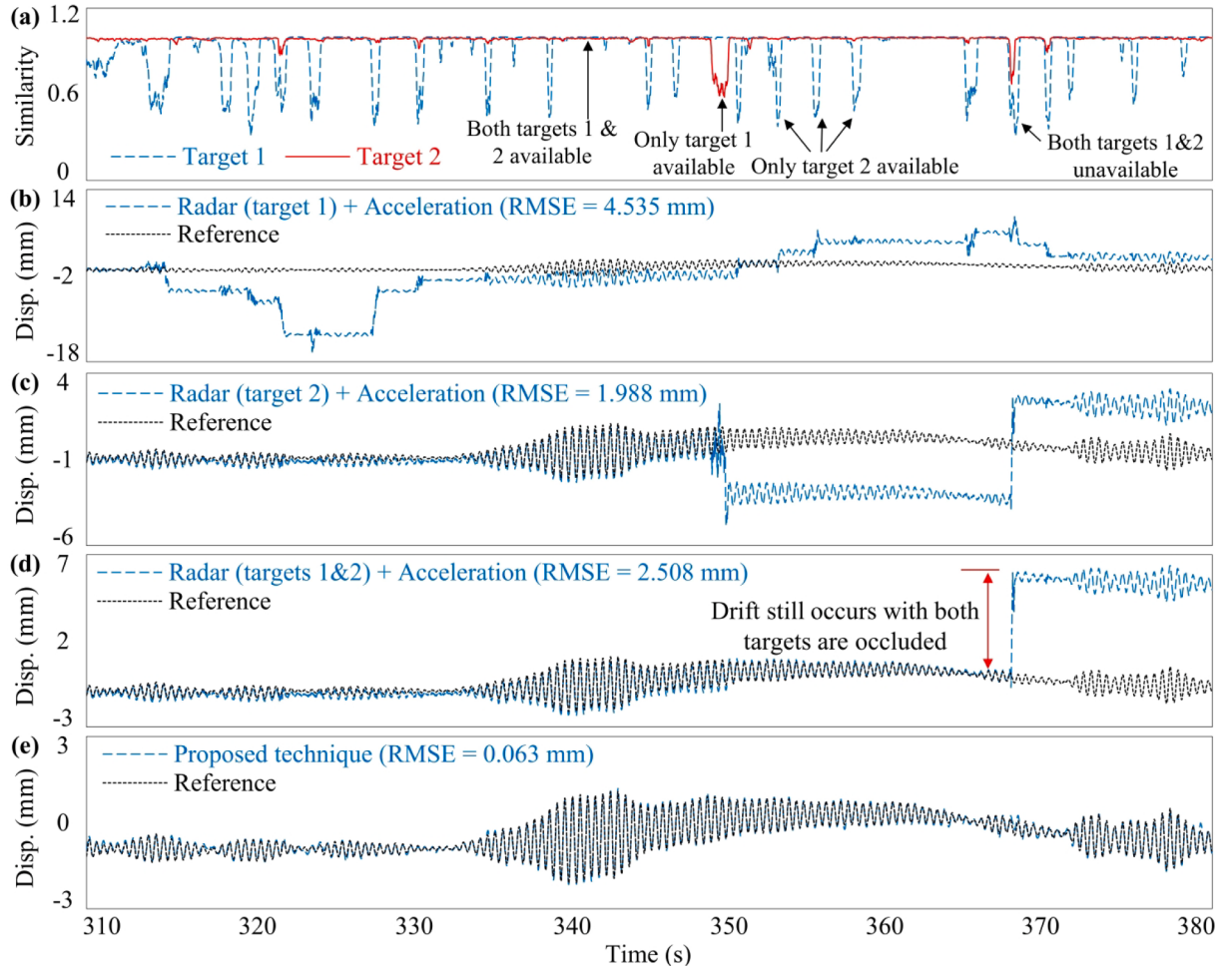
The test lasted for 600 s. Fig. 29 shows the amplitude spectrum, similarity scores, and unwrapped phases. Target 1, located on the right side of the road, is frequently occluded because of heavy traffic flow. Owing to the red light period, the target occlusion period for target 1 was up to 70 s; target 2, located on the right side of the road, was rarely occluded. Owing to intermittent target occlusion, the unwrapped phases extracted from both the targets have considerably large drifts (Fig. 30).

Fig. 30 shows displacement estimation procedure step by step for the time period from 310 s to 380 s. Intermittent target occlusion occurs for both targets as shown in Fig. 30(a). The displacements estimated from each of the two targets experience large drifts (Fig. 30(b) and (c)). The use of both targets removed displacement drifts caused by the occlusion of a single target; however, it did not remove the displacement drift caused by the occlusion of the two targets (Fig. 30(d)). The drift was removed by further fusing strain measurement, and the displacement was estimated accurately, as shown in Fig. 30(e). The acceleration was also used for phase unwrapping while estimating displacement from the radar measurement.

Fig. 31 compares the displacements estimated by (1) the fusion of strain and acceleration and (2) the fusion of millimeter-wave radar, acceleration, and strain (the proposed technique) for 600 s. Displacement is better estimated using the proposed technique, with an RMSE of less than 0.1 mm. The estimated displacement, zoomed into three different periods ([23 s, 33 s], [100 s, 110 s], and [430 s 440 s]), clearly indicates a better agreement between the displacement estimated by the proposed technique and reference displacement.



**Fig. 29.** Estimation results from radar measurement: (a) amplitude spectrum, (b) similarity scores for targets 1 and 2, and (c) unwrapped phase of targets 1 and 2.



**Fig. 30.** Estimation results from radar measurement from 310 s to 380 s: (a) similarity score for target 1 (blue dot line) and target 2 (black solid line), (b) displacement estimated using radar (target 1) and acceleration measurements, (c) displacement estimated using radar (target 2) and acceleration measurements, (d) displacement estimated using both targets 1 and 2, and (e) displacement estimated using radar (both targets 1 and 2), acceleration, and strain measurements. (For interpretation of the references to colour in this figure legend, the reader is referred to the web version of this article.)

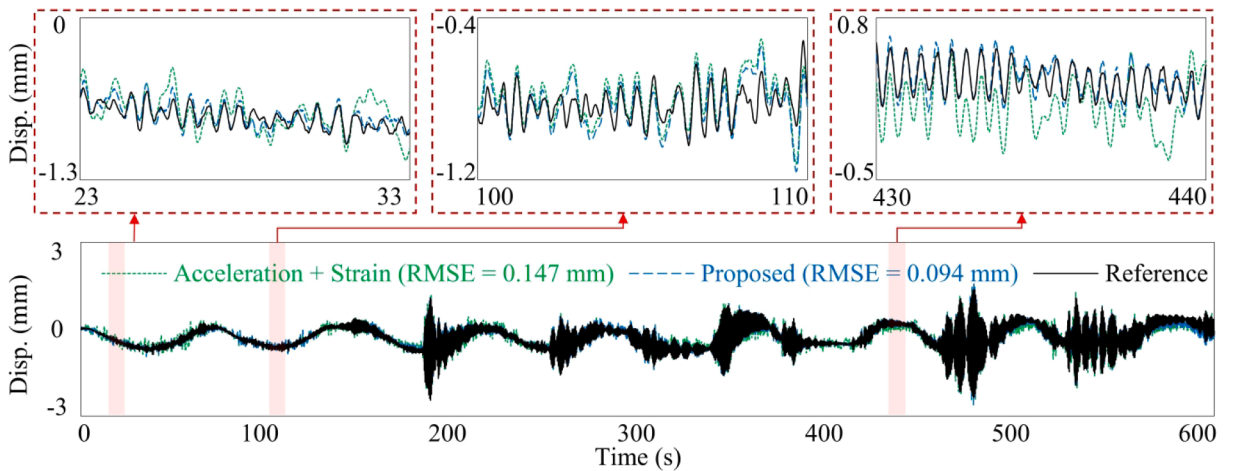


**Fig. 31.** Displacements estimated using (1) strain and acceleration radar measurements and (2) strain, acceleration, and radar measurements.

## 6. Conclusions

This study proposed a high-accuracy displacement estimation technique specifically for the long-term continuous measurement of the vertical movement of a bridge structure through the fusion of collocated accelerometer, strain gauge, and millimeter-wave radar on a target bridge. An automated initial calibration was first performed to (1) select the good targets among all targets detected by radar from the surroundings of the bridge and estimate conversion factors for the selected targets, and (2) train an ANN model for strain–displacement transformation. Subsequently, the displacement was continuously estimated by automated switching between the fusion of strain and acceleration and fusion of radar and acceleration, considering the intermittent radar target occlusion. The proposed technique offers the following advantages: (1) the continuous displacement estimation robust to intermittent radar target occlusion, (2) automated radar target occlusion detection and switching, and (3) reliable displacement estimation, even during the radar target occlusion period. The displacement estimation performance of the proposed technique was experimentally validated on a 10-m-long beam-type structure and steel box-girder pedestrian bridge. In both the tests, displacements were accurately estimated with RMSEs of approximately 0.1 mm, indicating the potential of the proposed technique in real-world bridge displacement monitoring, especially for mid- and small-span bridges.

The proposed technique aims at long-term bridge displacement monitoring, then the real-time displacement estimation performance is crucial for the proposed technique. However, in both experiments presented in the study, sensor measurements were pre-recorded and then the displacements were estimated by post-processing on a desktop computer. Therefore, the feasibility of the proposed technique for real-time bridge displacement estimation has not been fully validated. Efforts are underway to develop a low-cost displacement sensor consisting of a millimeter-wave radar, an accelerometer, a strain gauge, and a microcontroller for real-time displacement estimation. In addition, the proposed technique trained an ANN model to map the strain–displacement relationship using initial short-period sensor measurements, but this relationship may be time-variant, especially for long-term displacement monitoring. Future work will focus on the development of an online ANN model update algorithm.

## Declaration of Competing Interest

The authors declare that they have no known competing financial interests or personal relationships that could have appeared to influence the work reported in this paper.

## Data availability

Data will be made available on request.

## Acknowledgments

This study was supported by the National Research Foundation of Korea (NRF) grant funded by the Korean Government (MSIT) (No. 2017R1A5A1014883).

## References

- [1] Z. Sun, D.M. Siringoringo, Y. Fujino, Load-carrying capacity evaluation of girder bridge using moving vehicle, *Eng. Struct.* 229 (2021), 111645, <https://doi.org/10.1016/j.engstruct.2020.111645>.
- [2] S. Bhowmick, S. Nagarajaiah, Spatiotemporal compressive sensing of full-field Lagrangian continuous displacement response from optical flow of edge: Identification of full-field dynamic modes, *Mech. Syst. Sig. Process.* 164 (2022), 108232, <https://doi.org/10.1016/j.ymssp.2021.108232>.
- [3] L. Felipe-Sesé, F.A. Díaz, Damage methodology approach on a composite panel based on a combination of Fringe Projection and 2D Digital Image Correlation, *Mech. Syst. Sig. Process.* 101 (2018) 467–479, <https://doi.org/10.1016/j.ymssp.2017.09.002>.
- [4] A. Martini, E.M. Tronci, M.Q. Feng, R.Y. Leung, A computer vision-based method for bridge model updating using displacement influence lines, *Eng. Struct.* 259 (2022), 114129, <https://doi.org/10.1016/j.engstruct.2022.114129>.
- [5] K.V. Santhosh, B.K. Roy, Online implementation of an adaptive calibration technique for displacement measurement using LVDT, *Appl. Soft Comput.* 53 (2017) 19–26, <https://doi.org/10.1016/j.asoc.2016.12.032>.
- [6] D. Hester, J. Brownjohn, M. Bocian, Y. Xu, Low cost bridge load test: Calculating bridge displacement from acceleration for load assessment calculations, *Eng. Struct.* 143 (2017) 358–374, <https://doi.org/10.1016/j.engstruct.2017.04.021>.
- [7] M. Gindy, R. Vaccaro, H. Nassif, J. Velde, A state-space approach for deriving bridge displacement from acceleration, *Comput.-Aided Civ. Infrastruct. Eng.* 23 (2008) 281–290, <https://doi.org/10.1111/j.1467-8667.2007.00536.x>.
- [8] A.I. Ozdagli, B. Liu, F. Moreu, Low-cost, efficient wireless intelligent sensors (LEWIS) measuring real-time reference-free dynamic displacements, *Mech. Syst. Sig. Process.* 107 (2018) 343–356.
- [9] S. Shin, S.-U. Lee, Y. Kim, N.-S. Kim, Estimation of bridge displacement responses using FBG sensors and theoretical mode shapes, *Struct. Eng. Mech.* 42 (2012) 229–245, <https://doi.org/10.12989/sem.2012.42.2.229>.
- [10] Q. Zhang, J. Zhang, W. Duan, Z. Wu, Deflection distribution estimation of tied-arch bridges using long-gauge strain measurements, *Struct. Control Health Monit.* 25 (3) (2018) e2119.
- [11] S. Nakamura, GPS measurement of wind-induced suspension bridge girder displacements, *J. Struct. Eng.* 126 (2000) 1413–1419, [https://doi.org/10.1061/\(ASCE\)0733-9445\(2000\)126:12\(1413\)](https://doi.org/10.1061/(ASCE)0733-9445(2000)126:12(1413)).
- [12] J.R. Vazquez-Ontiveros, G.E. Vazquez-Becerra, J.A. Quintana, F.J. Carrion, G.M. Guzman-Acevedo, J.R. Gaxiola-Camacho, Implementation of PPP-GNSS measurement technology in the probabilistic SHM of bridge structures, *Measurement* 173 (2021), 108677, <https://doi.org/10.1016/j.measurement.2020.108677>.
- [13] P.L. Reu, D.P. Rohe, L.D. Jacobs, Comparison of DIC and LDV for practical vibration and modal measurements, *Mech. Syst. Sig. Process.* 86 (2017) 2–16, <https://doi.org/10.1016/j.ymssp.2016.02.006>.

- [14] C. Gentile, G. Bernardini, Output-only modal identification of a reinforced concrete bridge from radar-based measurements, *NDT and E Int.* 41 (2008) 544–553, <https://doi.org/10.1016/j.ndteint.2008.04.005>.
- [15] G. Zhang, Y. Wu, W. Zhao, J. Zhang, Radar-based multipoint displacement measurements of a 1200-m-long suspension bridge, *ISPRS J. Photogramm. Remote Sens.* 167 (2020) 71–84, <https://doi.org/10.1016/j.isprsjprs.2020.06.017>.
- [16] D. Lydon, M. Lydon, S. Taylor, J.M. Del Rincon, D. Hester, J. Brownjohn, Development and field testing of a vision-based displacement system using a low cost wireless action camera, *Mech. Syst. Sig. Process.* 121 (2019) 343–358, <https://doi.org/10.1016/j.ymssp.2018.11.015>.
- [17] R. Yang, S. Wang, X. Wu, T. Liu, X. Liu, Using lightweight convolutional neural network to track vibration displacement in rotating body video, *Mech. Syst. Sig. Process.* 177 (2022), 109137, <https://doi.org/10.1016/j.ymssp.2022.109137>.
- [18] E. Cai, Y. Zhang, Gaussian mixture model based phase prior learning for video motion estimation, *Mech. Syst. Sig. Process.* 175 (2022), 109103, <https://doi.org/10.1016/j.ymssp.2022.109103>.
- [19] Y.H. Hong, S.G. Lee, H.S. Lee, Design of the FEM-FIR filter for displacement reconstruction using accelerations and displacements measured at different sampling rates, *Mech. Syst. Sig. Process.* 38 (2013) 460–481, <https://doi.org/10.1016/j.ymssp.2013.02.007>.
- [20] K. Kim, H. Sohn, Dynamic displacement estimation by fusing LDV and LiDAR measurements via smoothing based Kalman filtering, *Mech. Syst. Sig. Process.* 82 (2017) 339–355, <https://doi.org/10.1016/j.ymssp.2016.05.027>.
- [21] F. Moschas, S. Stiros, Measurement of the dynamic displacements and of the modal frequencies of a short-span pedestrian bridge using GPS and an accelerometer, *Eng. Struct.* 33 (2011) 10–17, <https://doi.org/10.1016/j.engstruct.2010.09.013>.
- [22] K. Kim, J. Choi, J. Chung, G. Koo, I.-H. Bae, H. Sohn, Structural displacement estimation through multi-rate fusion of accelerometer and RTK-GPS displacement and velocity measurements, *Measurement* 130 (2018) 223–235, <https://doi.org/10.1016/j.measurement.2018.07.090>.
- [23] Z. Ma, J. Choi, H. Sohn, Real-time structural displacement estimation by fusing asynchronous acceleration and computer vision measurements, *Comput.-Aided Civ. Infrastruct. Eng.* 37 (2022) 688–703, <https://doi.org/10.1111/mice.12767>.
- [24] Z. Ma, J. Choi, P. Liu, H. Sohn, Structural displacement estimation by fusing vision camera and accelerometer using hybrid computer vision algorithm and adaptive multi-rate Kalman filter, *Autom. Constr.* 140 (2022), 104338, <https://doi.org/10.1016/j.autcon.2022.104338>.
- [25] Z. Ma, J. Chung, P. Liu, H. Sohn, Bridge displacement estimation by fusing accelerometer and strain gauge measurements, *Struct. Control Health Monit.* 28 (2021) e2733, <https://doi.org/10.1002/stc.2733>.
- [26] H. Zhu, K. Gao, Y. Xia, F. Gao, S. Weng, Y. Sun, Q. Hu, Multi-rate data fusion for dynamic displacement measurement of beam-like supertall structures using acceleration and strain sensors, *Struct. Health Monitor. Internat. J.* 19 (2020) 520–536, <https://doi.org/10.1177/1475921719857043>.
- [27] Z. Ma, J. Choi, L. Yang, H. Sohn, Structural displacement estimation using accelerometer and FMCW millimeter wave radar, *Mech. Syst. Sig. Process.* 182 (2023), 109582, <https://doi.org/10.1016/j.ymssp.2022.109582>.
- [28] J. Lee, S. Jeong, H. Kim, K.C. Lee, S.-H. Sim, Comparative study of long-term displacement measurement methods – Focusing on a Pre-stressed concrete bridge under construction, *Measurement* 201 (2022), 111691, <https://doi.org/10.1016/j.measurement.2022.111691>.
- [29] J. Guo, Y. He, C. Jiang, M. Jin, S. Li, J. Zhang, R. Xi, Y. Liu, Measuring micrometer-level vibrations with mmwave radar, *IEEE Trans. Mob. Comput.* 22 (4) (2023) 2248–2261.
- [30] R.E. Alva, L.G. Pujades, R. González-Drigo, G. Luzi, O. Caselles, L.A. Pinzón, Dynamic monitoring of a mid-rise building by real-aperture radar interferometer: advantages and limitations, *Remote Sens. (Basel)* 12 (2020) 1025, <https://doi.org/10.3390/rs12061025>.
- [31] D.V.Q. Rodrigues, D. Zuo, C. Li, Wind-induced displacement analysis for a traffic light structure based on a low-cost doppler radar array, *IEEE Trans. Instrum. Meas.* 70 (2021) 1–9, <https://doi.org/10.1109/TIM.2021.3098380>.
- [32] S. Guan, J.A. Rice, C. Li, Y. Li, G. Wang, Structural displacement measurements using DC coupled radar with active transponder, *Struct. Control Health Monit.* 24 (2017) e1909.
- [33] S. Guan, J.A. Bridge, C. Li, N.J. DeMello, Smart radar sensor network for bridge displacement monitoring, *J. Bridg. Eng.* 23 (2018) 04018102.
- [34] J.-W. Park, D.-S. Moon, H. Yoon, F. Gomez, B.F. Spencer Jr, J.R. Kim, Visual–inertial displacement sensing using data fusion of vision-based displacement with acceleration, *Struct. Control Health Monit.* 25 (2018) e2122.
- [35] Z. Ma, J. Choi, J. Jang, O. Kwon, H. Sohn, Y. Yang, Simultaneous estimation of submerged floating tunnel displacement and mooring cable tension through FIR filter based strain and acceleration fusion, *Struct. Control Health Monit.* 2023 (2023) 7803876, <https://doi.org/10.1155/2023/7803876>.
- [36] P. Ramasamy, S.S. Chandel, A.K. Yadav, Wind speed prediction in the mountainous region of India using an artificial neural network model, *Renew. Energy* 80 (2015) 338–347, <https://doi.org/10.1016/j.renene.2015.02.034>.
- [37] A.M. Zain, H. Haron, S. Sharif, Prediction of surface roughness in the end milling machining using Artificial Neural Network, *Expert Syst. Appl.* 37 (2010) 1755–1768, <https://doi.org/10.1016/j.eswa.2009.07.033>.
- [38] R. Lyons, *Understanding Digital Signal Processing*, 3rd ed., Pearson, Upper Saddle River, NJ, 2010.
- [39] L. Rabiner, R. Schafer, C. Rader, The chirp z-transform algorithm, *IEEE Trans. Audio Electroacoust.* 17 (1969) 86–92, <https://doi.org/10.1109/TAU.1969.1162034>.